Journal of Materials Chemistry A

PAPER

View Article Online
View Journal | View Issue

Published on 09 May 2014. Downloaded by Zhejiang Sci Tech University on 09/07/2014 13:10:12.

Cite this: J. Mater. Chem. A, 2014, 2, 11728

Probing the unexpected behavior of AuNPs migrating through nanofibers: a new strategy for the fabrication of carbon nanofiber–noble metal nanocrystal hybrid nanostructures†

Han Zhu,[a] MingLiang Du,*[ab] Ming Zhang,[ab] MeiLing Zou,[a] TingTing Yang,[a] LiNa Wang,[b] JuMing Yao[ab] and BaoChun Guo[c]

Received 3rd April 2014
Accepted 9th May 2014

DOI: 10.1039/c4ta01624f

www.rsc.org/MaterialsA

The intimate relationship of electrochemical sensors with high sensitivity and reliability has stimulated intensive research on developing versatile materials with excellent electrocatalytic activity. Here, we reported a novel strategy for the design of novel nanostructure-based electrochemical biosensors originating from an unexpected behavior of Au nanoparticles (AuNPs) embedded in the interior of polyacrylonitrile nanofibers (Au–PANFs), which can migrate to the external surfaces of the carbon nanofibers (Au–CNFs) during the graphitization process. Small and uniform AuNPs embedded in PANFs were synthesized *via* a combination of electrospinning and *in situ* reduction. With the conversion from the amorphous structures of PANFs to graphene layered structures of CNFs, the AuNPs can migrate from the interior of PANFs to the external surfaces of CNFs. The migration of AuNPs through the nanofiber matrix is strongly dependent on the graphitization temperature and heating rates. Three different heating rates of 2, 5, and 10 °C min^{-1} and graphitization temperatures of 600, 800, and 1000 °C were employed to investigate the migration and the exposed density of AuNPs on the CNFs. These novel nanomaterials were constructed as a nonenzymatic H_2O_2 electrochemical sensor and the sensors based on Au–CNFs with increased density of exposed AuNPs exhibit significantly promoted electrochemical activity. The Au–CNFs (1000 °C, 2 °C min^{-1}) with high exposed density and small sizes of AuNPs possess higher specific surface area and active sites, leading to higher electrocatalytic activity. The present investigations provide a general route for the fabrication of nanostructures for novel electrochemical sensors, energy storage devices and so on.

Introduction

Over the last two decades, the development of new electronic devices for wide applications in the sensitive detection of clinical, environmental, and food safety is currently an area of intensive research.[1,2] In this context, materials with dimensions at the nanoscale appear highly promising due to their exciting physical and chemical properties for the selective detection with low limits. Nanomaterial-based sensors exhibit extremely high surface area to volume ratio, which can increase the number of binding sites available for biological recognition element immobilization.[3–6] In addition, the utilization of nanomaterials usually leads to faster mass transfer rates, resulting in lower limits of detection and faster analyte detection rates than those seen in conventional sensors.[5,7,8]

Large amounts of nanomaterials, such as noble metal NPs, carbon nanotubes (CNTs) and graphene, are employed to construct the electrochemical biosensors.[9–14] Electrochemical detection of biomolecules using nanomaterials can often achieve high sensitivity because nanomaterials are extremely sensitive to electronic perturbations in the surrounding environment. Considerable efforts were devoted to novel nanomaterials to coordinate mass- and charge-transport and electron-transfer kinetics for realizing simultaneous minimization of primary resistances in biosensing: electrochemical reaction occurring at electrolyte/electrode interface, mass transport of analyte in electrolyte and electrode, and the electron conduction in electrode and current collector.[1,12–14]

Carbonaceous materials, such as CNTs and graphene, are of enormous interest, mainly due to their superior electrocatalytic activity for various chemical and biological systems.[15–17] The

[a]Department of Materials Engineering, College of Materials and Textile, Zhejiang Sci-Tech University, Hangzhou 310018, P. R. China. E-mail: du@zstu.edu.cn; Tel: +86-571-86843255

[b]Key Laboratory of Advanced Textile Materials and Manufacturing Technology, Zhejiang Sci-Tech University, Ministry of Education, Hangzhou 310018, P. R. China

[c]Department of Polymer Materials and Engineering, South China University of Technology, Guangzhou 510640, P. R. China

† Electronic supplementary information (ESI) available. See DOI: 10.1039/c4ta01624f

This journal is © The Royal Society of Chemistry 2014

Published on 09 May 2014. Downloaded by Zhejiang Sci Tech University on 09/07/2014 13:10:12.

control of heterogeneous electron-transfer kinetics through judicious design and structural manipulation of advanced carbon materials is of importance in the fabrication of many electrochemical devices such as biosensors.[8,15] Several groups have demonstrated the successful fabrication of sensitive biosensors using CNTs and graphene.[16–19] These sensors utilize the fast mass transfer and large surface areas provided by the carbonaceous nanomaterials. Myung *et al.* have reported the construction of a graphene-encapsulated nanoparticle-based biosensor for the selective detection of cancer biomarkers.[9] Chen *et al.* have fabricated the CNT-based electrochemical devices for the electronic sensing of proteins.[10]

Up to date, one-dimensional electrospun carbon nanofibers (CNFs) have been widely used as ideal electron pathways because of their intriguing chemical and physical properties such as good conductivity ($\rho = (3–7) \times 10^{-3}$ Ω cm).[17,20–23] Electrospinning is a highly versatile method to produce nanofibers of various polymers with diameters ranging from a few tens of nanometers to a few micrometers in different forms such as nonwoven mats, yarns, *etc.*[21–23] It is a relatively simple and low-cost strategy to produce continuous nanofibers from polymer solutions or melts. CNFs synthesized *via* electrospinning and subsequent graphitization had attracted attention mainly because their structures and properties can be easily adjusted by changing the processing conditions. Similar to other carbonaceous materials, electrospun CNFs are mostly used in the electrochemical applications related to the energy storage devices including lithium-ion batteries, supercapacitors, and fuel cells.[24–27] Only a few studies focus on the electrochemical sensor applications of the electrospun CNFs. In addition, the electrocatalytic activities of CNFs are often adjusted through the utilization of additional active components, such as loading or deposition of metal NPs onto the nanofibers.

Combining different materials with precise control of their interface at the nanoscale would lead to significantly enhanced properties. Noble metal nanostructures, especially Au nanostructures, have proven to be the most intriguing platforms suitable for a broad spectrum of bioapplications due to their bioinertness and biocompatibility, relatively simple and facile synthetic control and bioconjugation.[1,8,15] Recent years have witnessed tremendous efforts devoted to the design and synthesis of Au nanostructures in the application of electrochemical biosensors.[1,16] Au nanostructure-based electrochemical biosensors are extremely sensitive to the sizes, shapes and dispersion of Au nanostructures.[15,18,28,29] Recently, our group has reported the designs of noble metal nanostructure decorated one-dimensional organic nanofibers, employing as the electrochemical biosensors for the detection of H_2O_2, glucose and glutathione.[30–33] Small sizes of Au nanocrystals usually can dramatically influence their physical and chemical properties arising from their large surface-area-to-volume ratio and the spatial confinement of electrons, phonons, and electric fields in and around these particles.[30,31] These novel nanocrystal–nanofiber hybrid architectures exhibit high surface area and strong electrochemical activities, leading to advanced materials for electrochemical sensors, nanoelectronics, energy storage devices and catalysts.

Unlike organic nanofibers, CNFs lack functional groups and are consequently relatively chemically inert. Common strategies to decorate the CNFs with nanocrystals include surface treatments by ultrasonication and acid-assisted oxidation, vapor deposition and solution growth.[34–36] Hermans *et al.* have reported that CNTs and CNFs functionalized with HNO_3 can produce surface carboxyl groups, serving as anchoring points for the grafting of PdNPs.[37] Liang *et al.* have synthesized PdNP functionalized CNF composites through a two-step chemical vapor deposition of Pd(allyl)(Cp).[38] However, because of the complex interfacial reactions involved and more demanding process conditions imposed, the size and distribution control of nanocrystals on CNFs become considerable problems. How to synthesize excellent electrochemical sensors based on CNFs incorporated with small and uniform nanocrystals still remains a huge challenge.

Recently, Yang *et al.* have reported an approach to prepare CNFs decorated with SnO_2 nanocrystals by combining the PANFs and stannous chloride salt solution.[39] After the carbonization in an Ar/H_2O atmosphere, the SnO_2-NPs were formed on the surfaces of the CNFs. Similarly, Hou *et al.* prepared the PANFs mixed with Fe(acetylacetonate)$_3$ to synthesize CNF/Fe nanocomposites and the FeNPs immobilized on the CNFs can serve as the catalysts for the growth of CNTs.[40]

Unlike the above common strategies and newly raised thermal decomposition approaches, we proposed a new strategy and synthesized a new system, CNF–Au nanostructures. In the procedure, accompanied with the conversion from PANFs to CNFs, the nanostructure of CNF–Au and can be assembled and tailored by the migration of AuNPs in PANFs to the outside of CNFs during the graphitization process. Our previous work has reported a green and facile approach for the synthesis of small and uniform AuNPs embedded in the interior of the PANFs *via* a combination of electrospinning and *in situ* reduction.[41,42] Note that intriguing phenomena can be observed during the graphitization process. With the conversion from the amorphous structures of PANFs to graphene layered structures of CNFs, the initial AuNPs migrate from the interior of PANFs to the exterior of CNFs. The migration of AuNPs through the nanofiber matrix is strongly dependent on the graphitization temperature and heating rates. We employed three different heating rates of 2, 5, and 10 °C min^{-1} and graphitization temperatures of 600, 800, and 1000 °C, respectively, to investigate the migration and the exposed density of AuNPs on the CNFs. The conversion from embedded AuNPs to exposed AuNPs attached to the external surfaces of CNFs is explained by an atom diffusion mechanism. In addition, we also investigate the conversion in the chemical structures from the –C≡N structure to the –C=C–C=N structure during the graphitization process. Similar phenomena can be obtained by Pt–CNF hybrid nanostructures, indicating that this new strategy will provide a general approach for the fabrication of CNF–noble metal nanostructures. These novel nanomaterials were constructed as a nonenzymatic H_2O_2 electrochemical sensor. The electrochemical sensors based on Au–CNFs with increased density of exposed AuNPs exhibit significantly promoted electrochemical activity with increased density of exposed AuNPs. The Au–CNFs with high density of

Published on 09 May 2014. Downloaded by Zhejiang Sci Tech University on 09/07/2014 13:10:12.

exposed AuNPs possess higher specific surface area and active sites. It means that more AuNPs will take part in the reactions, leading to higher electrocatalytic activity. The sensors show a lower detection limit and wider responding range, indicating that the fabricated sensor could be potentially used for monitoring the concentration of H_2O_2 without any enzyme.

Experiment section

Materials and methods

Materials. Chloroauric acid ($HAuCl_4 \cdot 4H_2O$, 99.9%), hydrogen per-oxide (30%), hydroquinone (HQ), phosphate buffered saline (PBS) and dimethyl formamide (DMF, 99.5%) were commercially available from Shanghai Civi Chemical Technology Co., Ltd. Polyacrylonitrile (PAN, $M_w \approx 1.4 \times 10^5$, copolymerized with 10 wt% methyl acrylate) was manufactured by Sinopec Shanghai Petrochemical Co., Ltd. Epigallocatechingallate (EGCG, 98%) were purchased from XuanChengBaiCao Plant Industry and Trade Co., Ltd. All of the chemicals were used without further purification. Deionized water (DIW, 18.2 MΩ) was used for all solution preparations.

Synthesis of Au–PANF precursor solution. The first step involved the synthesis of AuNPs in PAN/DMF solution *via* an *in situ* reduction method.[41] Briefly, 6 g PAN powder was dissolved in 44 mL DMF under magnetic stirring at 65 °C to get a homogenous solution. Then, 0.30 mmol $HAuCl_4 \cdot 4H_2O$ was added to the PAN/DMF solution and the mixture were stirred at 65 °C for 1 h. Finally, 0.025 g EGCG was immediately added to the above mixture and the mixture was stirred using a magnetic agitator for 3 h. Therefore, the mass fraction of PAN in the DMF solution was 12 wt% and the mass ratio of $HAuCl_4 \cdot 4H_2O$ and the PAN powder was 1.0 wt%.

Fabrication of PANF and Au–PANF nanofibrous mats. The PAN/DMF (12%) and Au–PANF precursor solution with the mass ratio of 1.0 wt% ($HAuCl_4 \cdot 4H_2O$ to PAN) was used to prepare nonwoven mats *via* an electrospinning technique. The precursor solution was transferred into a syringe with a stainless copper needle at the tip. The needle was connected to a high voltage power supply. The applied voltage was 12 kV, the needle to collector distance was 12 cm and the flow rate of the solution was 0.6 mL h^{-1}. All experiments were performed at room temperature. The electrospun PANF and Au–PANF nanofibrous mats were collected onto a piece of aluminum foil.

Fabrication of CNF and Au–CNF nanofibrous mats. The as-collected electrospun PANF and Au–PANF nanofibrous mats were peeled off from the aluminum foil and placed into a home-built CVD tube furnace for heat treatment. The nanofibrous mats were heated to 280 °C in air at a rate of 5 °C min^{-1} and maintained for 6 h for stabilization, then the samples were heated up to 800 °C at a rate of 5 °C min^{-1} under Ar gas flow (50 Sccm) for the graphitization. The desired graphitization temperature was held constant for 8 h and then the products were cooled to room temperature under an Ar atmosphere.

Fabrication of Au–CNF nanofiber biosensors for H_2O_2 detection. For the fabricating procedure of the Au–CNF/GCE biosensor, the glassy carbon electrode (GCE) with a diameter of 3 mm was polished carefully using alumina slurry as a polisher to get a mirror-like surface, followed by rinsing with DIW and ethanol and then drying with nitrogen. The Au–CNF fibrous mat was glued by Nafion aqueous solution (1 wt%) on the pretreated GCE and left to dry by N_2 at room temperature. The modified electrode was washed gently with DIW and then soaked in PB at 4 °C. This modified electrode is denoted as Au–CNF/GCE. The control sample, CNFs, was fabricated using similar procedures for the preparation of CNF/GCE biosensors. All the modified electrodes were stored at 4 °C in a refrigerator before further characterizations.

Electrocatalytic measurement. Amperometric experiments were conducted with a CHI660H workstation (Shanghai Chenhua, Shanghai). All experiments were carried out using a conventional three-electrode system in 0.1 M PBS, where CNF/GCE and Au–CNF/GCE were used as the working electrode, a platinum foil as the auxiliary electrode and a saturated Ag/AgCl electrode as the reference electrode. The buffer was purged with high-purity nitrogen for at least 30 min prior to each amperometric experiment, and the nitrogen environment was then maintained over the solution to protect the solution from oxygen. Electrochemical performances of the fabricated electrodes were tested using a three-electrode system by cyclic voltammetry (CV).

Instrumentation. The morphology evolution of the PANFs, CNFs, Au–PANFs, Au–CNFs, Pt–PANFs and Pt–CNFs were characterized by JSM-2100 transmission electron microscopy (JEOL, Japan) at an acceleration voltage of 200 kV and JSM-6700F FE-SEM (JEOL, Japan) at an acceleration voltage of 3 kV. X-ray photoelectron spectra of the products were recorded using an X-ray photoelectron spectrometer (Kratos Axis Ultra DLD) with an aluminum (mono) K_α source (1486.6 eV). The aluminum K_α source was operated at 15 kV and 10 mA. Fourier transform infrared (FTIR) spectra were recorded on a Nicolet 5700 FTIR spectrometer in transmittance mode at a resolution of 4 cm^{-1} and 32 scans in the range from 4000 nm to 400 nm. XRD patterns of the nanofibrous mats were characterized with a SIEMENS Diffraktometer D5000 X-ray diffractometer using a Cu K_α radiation source at 35 kV, with a scan rate of 0.02° 2θ s^{-1} in the 2θ range of 10–80°. Raman spectra of all the samples were recorded using a RenishawinVia Raman microscope using a 532 nm laser excitation source. The excitation light intensity in front of the objective was 10 mW with a spectral collection time of 1 s. The integration time for our measurements was set to 10 s. The high-angle annular dark field scanning TEM (HAADF-STEM) image, STEM mapping and line-scan energy dispersive X-ray spectroscopy (EDX) images were recorded using a STEM (Tecnai G2 F30 S-Twin, Philips-FEI) at an acceleration voltage of 300 kV.

Results and discussion

The morphologies of the electrospun polyacrylonitrile nanofibers with embedded AuNPs (Au–PANFs) and carbon nanofibers with immobilized AuNPs on surfaces (Au–CNFs) were determined by using the FE-SEM and TEM characterizations. As shown in Fig. 1a, the distinct and continuous Au–PANFs are straight and have smooth surfaces with an average diameter of

 This journal is © The Royal Society of Chemistry 2014

Published on 09 May 2014. Downloaded by Zhejiang Sci Tech University on 09/07/2014 13:10:12.

about 512 ± 54 nm. The hybrid nanofibers are up to hundreds of micrometers in length, leading to high surface-to-volume ratios. In addition, no AuNPs can be seen on the surfaces of the Au–PANFs. However, from the TEM image of Au–PANFs shown in Fig. 1b, small AuNPs with an average diameter of 2.3 ± 0.5 nm are evenly dispersed in the whole PANFs, indicating that the AuNPs are mainly embedded in the interior of PANFs. In addition, the inset in Fig. 1b exhibits a HRTEM image of AuNPs, showing lattice fringes of the Au (111) plane with an interplanar distance of 0.23 nm.

Compared with the smooth surfaces of Au–PANFs, as shown in Fig. 1d, large amounts of AuNPs were immobilized on the surfaces of CNFs. It means that after the graphitization process, the initial AuNPs embedded in the interior of PANFs broke through the nanofiber and formed on the external surfaces of CNFs. The average diameter of the Au–CNFs decreases to 200 ± 44 nm after graphitization, indicating the significant shrinkage of the nanofibers. The TEM image of Au–CNFs exhibits small and uniform AuNPs distributed on CNFs and the lattice fringes shown in the inset in Fig. 1e are visible with a spacing of about 0.23 nm, which corresponds to the lattice spacing of the (111) planes of Au.[41] Meanwhile, after the graphitization treatment at 800 °C, the diameter of AuNPs formed on the surfaces of CNFs increased to 5.6 ± 0.7 nm and no aggregated NPs are observed.

The interfacial structures of Au–CNFs can be resolved in greater detail by HAADF-STEM imaging (Fig. 1c). The HAADF-STEM image of the Au–CNFs can also indicate that the AuNPs are evenly immobilized on the surfaces of CNFs. As shown in Fig. 1c and f, it is apparent that the brighter spots are the AuNPs, and the STEM-EDS mapping (Fig. 1g) demonstrates that the quasi-spherical shapes of the AuNPs are immobilized on the external surfaces. Compared with Fig. 1f, the positions of AuNPs in the mapping image (Fig. 1g) are nearly consistent with the AuNPs anchored on CNFs.

XRD patterns can provide much information about the crystal structures of Au–PANFs and Au–CNFs. As shown in Fig. 1h, the Au–PANF nanofibrous mats exhibit a sharp peak and a broad band, locating at 16.9° and 27.7°, which are ascribed to the PAN crystalline phase of the (110) plane and the amorphous phase.[43,44] However, no diffraction peaks of Au crystals emerged on the XRD pattern. Meanwhile, the representative diffraction peak (002) of the stacked graphite layers (JCPDS 75-1621) in the Au–CNFs is detected at $2\theta = 24.7°$, demonstrating the crystalline structures of graphitic carbon in the nanofibers.[45,46] Interplanar d-spacing of the graphite layers were calculated using Bragg's Law.[45,46] By using $\lambda = 0.154$ nm (Cu K_α), the calculated value of d_{002} of Au–CNFs is 3.60 Å. Compared with Au–PANFs, four new strong peaks appeared at 38.3°, 44.4°, 64.8°, and 77.8°, which are consistent with the (111), (200), (220) and (311) planes of Au crystals, respectively (JCPDS 04-0784).[47,48] The strong differences in the diffraction peaks of the Au crystals between the Au–PANFs and Au–CNFs

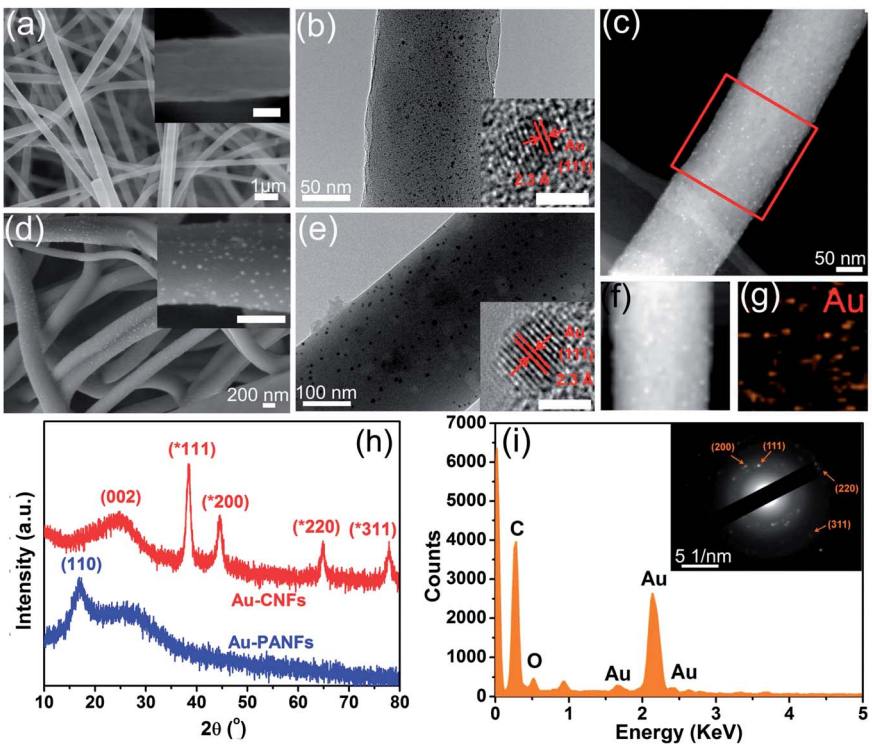

Fig. 1 FE-SEM and TEM images of the (a and b) Au–PANFs and (d and e) Au–CNFs graphitized at 800 °C. Insets in (a and d) are the high-magnification FE-SEM images of the Au–PANFs and Au–CNFs (scale bar 200 nm). Insets in (b and e) are the HRTEM images of the AuNPs embedded in PANFs and on the surfaces of CNFs, respectively (scale bar 2 nm). (c and f) HAADF-STEM images of the Au–CNFs and the (g) STEM-EDS mapping image of the selective area of Au–CNFs. (h) XRD patterns of the Au–PANF and Au–CNF nanofibrous mats. (i) EDX spectrum of the Au–CNFs. Inset in (i) is the SAED pattern of the Au–CNFs.

Published on 09 May 2014. Downloaded by Zhejiang Sci Tech University on 09/07/2014 13:10:12.

demonstrate that the Au–CNFs have much exposed AuNPs on the surfaces, which are consistent with the FE-SEM and STEM results. We have further preformed the EDX spectroscopy of Au–CNFs, and Fig. 1i shows the Au, C and O elements, confirming the presence of AuNPs. The SAED pattern (inset in Fig. 1i) recorded on the mapping region of Au–CNFs as indicated by the red square in Fig. 1c further verifies that the AuNPs are polycrystalline in nature and consist of face-centered cubic-phase nanocrystallines. The concentric diffraction rings from inside to outside are indexed to the (111), (200), (220), and (311) planes of Au crystals.[18,48]

XPS was used to investigate the chemical states of the surfaces of Au–PANFs and Au–CNFs. As shown in Fig. 2a, the Au 4f XPS spectra of Au–PANFs can be deconvoluted to two peaks at 88.0 and 84.3 eV, which are associated with the binding energies (BEs) of Au $4f_{7/2}$ and Au $4f_{5/2}$, respectively. Compared with the BEs of Au^0 (87.7 eV and 84.0 eV), the higher BEs of Au 4f indicate that the AuNPs embedded in PANFs are surrounded by the PAN molecules, leading to a substantial electron donation from AuNPs to the stabilizer molecules.[41,49,50] Tanaka and Negishi *et al.* have reported that the relatively high binding energy of Au 4f was due to the binding of surface Au atoms in AuNPs with the stabilizer or passive molecules surrounding the nanoparticles, which led to a substantial electron donation from AuNPs to the stabilizer molecules.[49,50] These indicate that the AuNPs were embedded in the interior of PANFs and surrounded by large amounts of PAN molecules.

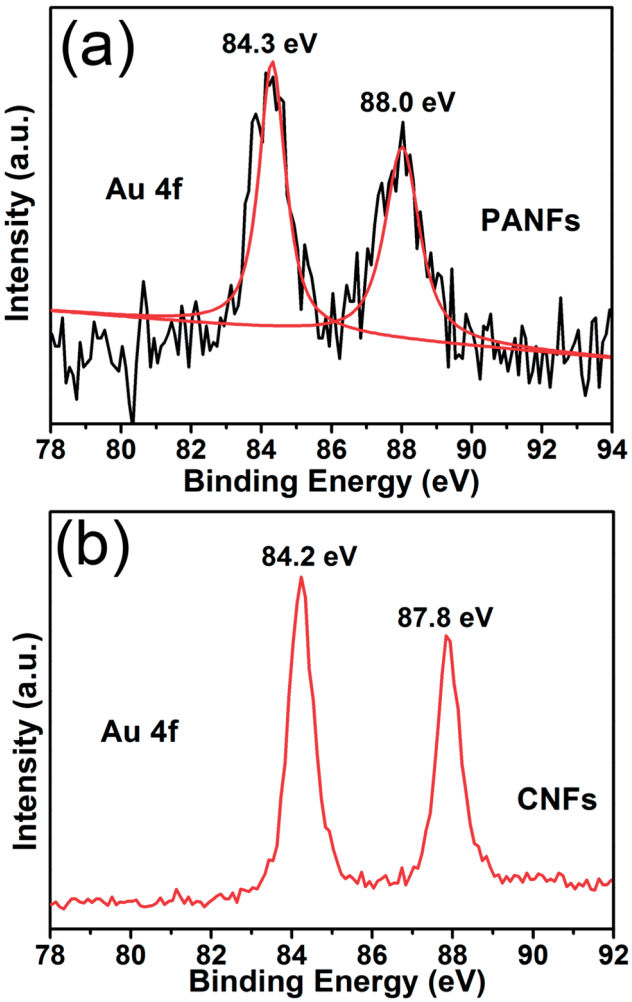

Fig. 2 XPS spectra of the Au 4f of (a) Au–PANFs and (b) Au–CNFs graphitized at 800 °C.

Focusing on the XPS spectrum of Au–CNFs, two sharp and distinct peaks can be observed at 84.2 and 87.8 eV. Compared with that of the Au–PANFs, the BEs of Au 4f of Au–CNFs are close to the BEs of Au^0, indicating that the AuNPs on the surfaces of CNFs are surrounded by few molecules. A few molecules around the exposed AuNPs on CNFs lead to weaker substantial electron donation, and the small changes in the BEs of Au 4f. The intensity of the Au 4f peaks of Au–CNFs is much higher than that of Au–PANFs, demonstrating that the Au–CNFs have more exposed AuNPs on the surfaces of the nanofibers. The XPS results are consistent with the FE-SEM, STEM and XRD results and more discussion can be found in the following studies.

To investigate the evolution of the AuNPs transferred from the interior to the external surfaces, we performed a control experiment to study the graphitization of the PANFs. The morphologies, microstructures and crystal structures were examined by TEM, FESEM, STEM, XRD and Raman characterizations. Fig. 3a shows the amorphous structure of PANFs and as shown in Fig. 3b, the carbonaceous matrix of CNFs was constructed by graphitic carbon layers. The insets in Fig. 3b show the lattice spacing of 0.36 nm corresponding to the (002) lattice plane of graphite and the typical diffraction pattern of the CNFs, reflecting randomly oriented polycrystallites.[45,46] Therefore, along with the carbonization from PANFs to CNFs, the amorphous structures of PANFs converted to the graphitic carbon layered structures.

The HAADF-STEM and STEM-EDS mapping images of CNFs clearly show three different elements, which are ascribed to carbon, oxygen and nitrogen. We have further performed line-scanned EDX spectroscopy on individual CNF. Fig. 3l shows the line-scanned EDX spectra of CNFs along the red-line (Fig. 3f) across the nanofiber, which clearly shows the existences of carbon, oxygen and nitrogen.

Comparing the FE-SEM images of PANFs with CNFs, the average diameters of nanofibers decreased from 560 nm to 200 nm, indicating the significant shrinkage of the PANFs. Based on the above results, we suppose that the AuNPs transferred from the interior of PANFs to the exterior of CNFs was caused by the carbonization process, and more experiments and discussion will be performed in the following studies. XRD patterns also indicate the structure conversion from PANFs to CNFs. As shown in Fig. 3j, the PANF mats exhibit two peaks, locating at 17.1° and 26.7°, which are ascribed to the PAN crystalline phase and the amorphous phase, respectively. The broader diffraction peaks of CNFs centered at 24.1° and 44.1° are attributed to carbon (002) and (100) planes. The d_{002} calculated value of pure CNFs is 3.69 Å. Compared with the d_{002} value of graphite (0.335 nm), the expanded d_{002} value of CNFs (0.369 nm) and Au–CNFs (0.360 nm) implies that the graphene layers are displaced due to many layer-sequential

 This journal is © The Royal Society of Chemistry 2014

Published on 09 May 2014. Downloaded by Zhejiang Sci Tech University on 09/07/2014 13:10:12.

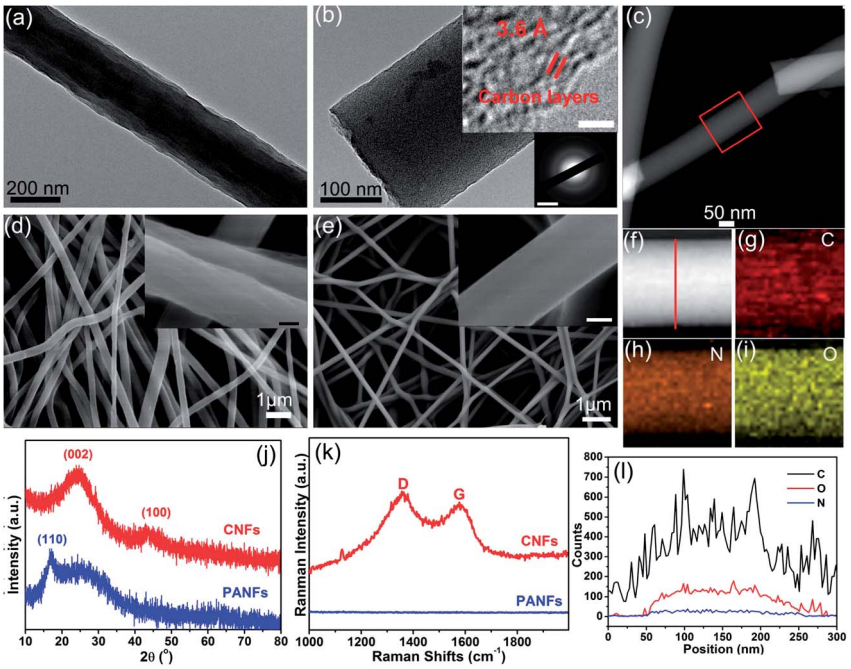

Fig. 3 TEM and FE-SEM images of the (a and d) PANFs and (b and e) CNFs graphitized at 1000 °C. (c and f) HAADF-STEM images of the Au–CNFs and the (g–i) STEM-EDS mapping images of the selective area of CNFs. (j) XRD patterns and (k) Raman spectra of the PANF and CNF nanofibrous mats. (l) Line-scan EDX spectra of the CNF. Insets in (b) are the HRTEM image and SAED pattern of the CNFs (scale bars, 2 nm and 5 nm^{-1}). Insets in (d and e) are the high-magnification FE-SEM images of CNFs (scale bars, 200 nm and 100 nm).

mismatches occurring in the CNFs and that there is much space for energy storage.[24,45,46]

The Raman spectrum of the PANFs does not show any peaks in the range from 1000 to 2000 cm^{-1}, while the CNFs exhibit two fundamental vibrations, which are observed at 1357 and 1577 cm^{-1}. The primary peak (D band) corresponds to the breaking symmetry caused by defects or structural disorders, while the later peak (G band) is related to in-plane tangential stretch vibration mode of the graphitic layer.[48,51] The intensity ratio of D and G bands (I_D/I_G) was calculated to be 1.09, showing that the CNFs indeed composed of graphitic rolls mixed with a small amount of amorphous carbon and a number of pores.

FTIR and XPS were used to study the evolution in chemical structures, surface compositions and chemical states of the PANFs and CNFs during the graphitization process. As shown in Fig. 4a, the FTIR spectra of PANFs, pre-oxidation PANFs at 280 °C (PANOF) and CNFs graphitized at 1000 °C were performed to investigate the evolution in chemical structures during the graphitization process.

The PANFs displays a broad band centered at 3472 cm^{-1} ascribed to the stretching vibration of O–H groups. The other three characteristic peaks at 1670, 2242 and 2931 cm^{-1} correspond to the C=O stretching in carboxylate groups, C≡N stretching in nitrile groups and C–H stretching in C–H and CH_2 groups, which are consistent with the previous literature.[41,43,52] After the pre-oxidation at 280 °C, the FTIR spectrum of PANOFs exhibits weaker intensity of C≡N peaks (2242 cm^{-1}). In addition, the two strong peaks located at 1590 and 1372 cm^{-1} are ascribed to the C=N and C=C stretching vibration and the C–H in-plane blending vibration, indicating the conversion

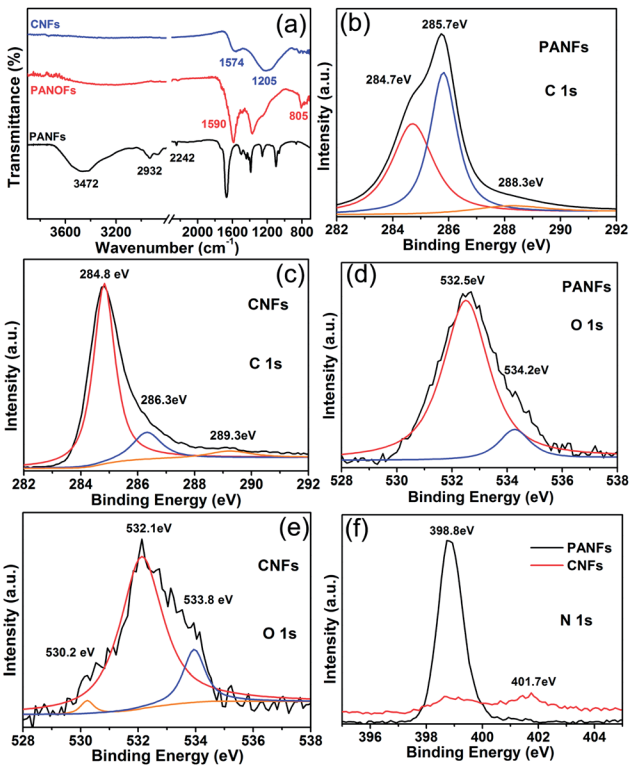

Fig. 4 (a) FTIR spectra of the PANFs, pre-oxidation PANFs at 280 °C and CNFs carbonized at 1000 °C. XPS spectra of C 1s of (b) PANFs and (c) CNFs. XPS spectra of O 1s of (d) PANFs and (e) CNFs. (f) XPS spectra of N 1s of PANFs and CNFs.

Published on 09 May 2014. Downloaded by Zhejiang Sci Tech University on 09/07/2014 13:10:12.

from the C≡N structure to the C=C–C=N structure during the pre-oxidation process.[52,53] What is more, a strong peak ascribed to the C=C–H bending vibration can be observed at 805 cm^{-1}. The above FTIR results demonstrate that the C≡N structures were converted to the C=C–C=N structure, forming the aromatic structures. After the carbonization at 800 °C, the characteristic peaks for O–H, C≡N are vanished, the peaks located at 1574 and 1205 cm^{-1} are attributed to the C=C or C=N stretching vibration and C–N bending vibration. Such chemical changes can clearly demonstrate the chemical structure conversion during the graphitization process.

The XPS spectra of PANF and CNF nanofibrous mats are shown in Fig. 4b–f. As shown in the C 1s spectra of PANFs in Fig. 4b, three different types of carbon with different chemical states are observed at 284.7, 285.7 and 288.3 eV, respectively. These peaks are ascribed to the carbon atoms in different functional groups: the C–C, the C in C≡N bonds and the C in C=O bonds, respectively.[53,54] Meanwhile, the CNFs show a distinct peak located at 284.8 eV corresponding to the graphitized carbon. The other two weaker peaks located at 286.3 and 289.3 eV are ascribed to the C–O or C–N bonds and C=O bonds. The C=O groups of PANFs are due to the two different chemical environments of oxygen in methyl acrylate (PAN contains 10 wt% of methyl acrylate), while the C=O groups of CNFs are due to the oxygen-containing groups on the surface of the nanofibers, which are similar to those of our previous studies.[41] The O 1s XPS spectra of PANFs exhibit two peaks at 532.5 eV and 534.2 eV associated with the chemical environments of oxygen in carbonyl groups of methyl acrylate. Focusing on the CNFs, the O 1s spectra show two peaks located at 530.2 and 532.1 eV may be due to adsorbed oxygen, and carbonyl groups.

The higher binding energy peak at 533.8 eV possibly originates from absorbed H_2O, which is similar to the previous reports.[53–55] The N 1s spectra of the PANFs exhibit a significant peak at 398.8 eV and it can be assigned to the nitrogen atoms that bond with carbon atoms in the form of C≡N bonds.[51] Meanwhile, after the graphitization process, the CNFs show two very weak bands centered at 399.0 eV and 401.7 eV, which are attributed to the C≡N species and pyridinic nitrogen, demonstrating the formation of the C=C–C=N structure. The above results confirm the conversion in the chemical structures from C≡N to C=C–C=N structure during the graphitization process. Based on the FTIR and XPS results, the conversion in chemical structures from PANFs to CNFs is illustrated in Fig. S1.† The graphitization processes for the conversion from PANFs to CNFs are divided into three steps: oxidative stabilization, high-temperature carbonization, and graphitization.[56] The stabilization of PANFs treated at 280 °C can ensure both the molecules and the molecular orientation. At this stage, the adjacent cyano groups reacted with each other and thus, the macromolecules cross-link together through the chemical bonds. Through the carbonization and graphitization process, the chemical structures covert from C≡N to C=C–C=N structure, forming the aromatic structure and then graphene layered structures.

Based on the above results, the graphitization process would lead to the significant shrinkages of the nanofibers and the structure conversions from amorphous to graphene layered structures. The high graphitization temperature and fast heating rate could lead to the dramatic shrinkage of the nanofibers, which are the key for the migration of AuNPs from the interior to the exterior of the nanofibers.

In the follow study, we performed the control experiments for the conversion from Au–PANFs to Au–CNFs with different graphitization temperatures and heating rates. As shown in Fig. 5a and e, the Au–PANFs with higher mass ratio of $HAuCl_4 \cdot 4H_2O$ (2.5 wt %) were synthesized to explore the migration and evolution of the AuNPs. As shown in Fig. 5a, large amounts of spherical AuNPs with an average diameter of about 2.5 ± 0.6 nm are evenly embedded in the interior of PANFs. From the edges of the PANFs (inset in Fig. 5a) and the FE-SEM image of the Au–PANFs, nearly no AuNPs can be observed at the surfaces of PANFs. After the graphitization at 600 °C, the average diameter of spherical AuNPs increases to 4.1 ± 1.1 nm and the AuNPs trend to migrate to the edges of the CNFs, which can be observed in Fig. 5b and f. From Fig. 5f, the FE-SEM image of Au–CNFs (600 °C, 2 °C min^{-1}) exhibits that a lot of AuNPs break through the CNFs and immobilize on the surfaces of CNFs. In addition, there is still space among the AuNPs and non-aggregated AuNPs.

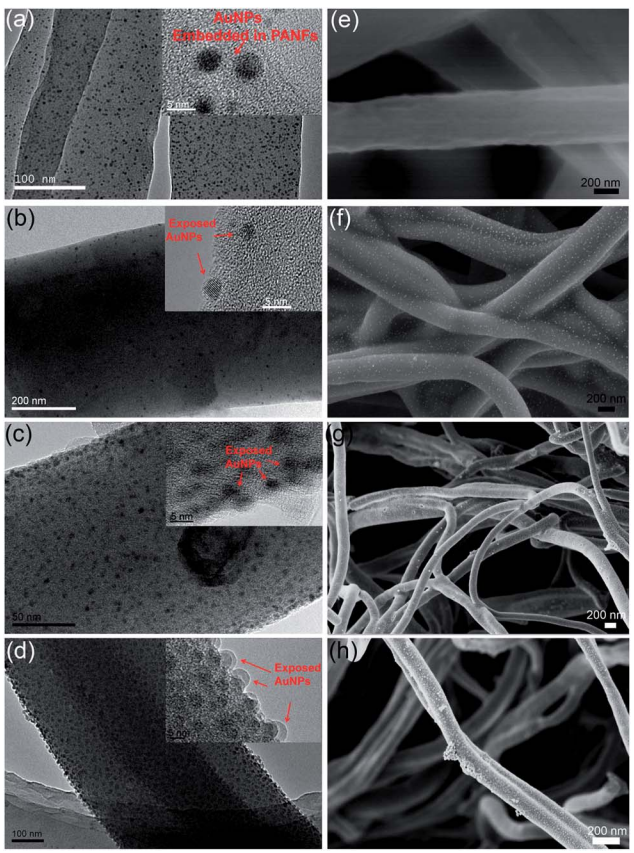

Fig. 5 (a) TEM and (e) FE-SEM images of the Au–PANFs with the mass ratio of 2.5 wt% (PAN and $HAuCl_4$). TEM and FE-TEM images of Au–CNFs with various graphitization temperatures at (b and f) 600 °C, (c and g) 800 °C and (a and h) 1000 °C, respectively. Insets are the corresponding HRTEM images of the Au–PANFs and Au–CNFs. The heating rate of the graphitization process is 2 °C min^{-1}.

This journal is © The Royal Society of Chemistry 2014

Published on 09 May 2014. Downloaded by Zhejiang Sci Tech University on 09/07/2014 13:10:12.

Meanwhile, the diameter of Au–PANFs is about 530 ± 52 nm while that of the Au–CNFs is about 320 ± 64 nm, indicating the significant shrinkage of the nanofibers. With an increased graphitization temperature of 800 °C, as shown in Fig. 5c and g, more and more spherical AuNPs can be found on the surfaces of CNFs and the distance among each AuNP becomes less. In addition, it can be seen from the HRTEM image (inset in Fig. 5c) of the edges of Au–CNFs that the AuNPs are emigrating from the interior of CNFs. The average diameter of the AuNPs increases to 4.9 ± 1.2 nm and the diameter of the Au–CNFs decreases to 260 ± 43 nm, indicating the continuous migration of AuNPs and shrinkage of the nanofibers. When the temperature increased to 1000 °C, most of the spherical AuNPs are exposed on the surfaces of the CNFs and the AuNPs are right next to each other (Fig. 5d). The average diameter of the AuNPs increased to 6.9 ± 1.4 nm and the diameter of the Au–CNFs decreased to 210 ± 45 nm. However, although large amounts of AuNPs formed, there were still no aggregated NPs, demonstrating that at the low heating rate, the Au–CNFs with a higher density of exposed AuNPs with small and uniform sizes can be obtained.

Table 1 summarizes the XPS atomic concentrations, mass concentrations and Au 4f BEs of the Au–PANFs and CNFs graphitized at 600, 800, and 1000 °C min^{-1} at a heating rate of 2 °C min^{-1}. In our present investigations, we used the same Au–PANF samples to prepare Au–CNF nanofibrous mats and it means that the mass concentration of Au in PANFs before graphitization is constant. The Au–PANFs exhibit the lowest atomic and mass concentrations of Au, which are 0.06 and 0.96%, suggesting the lowest density of exposed AuNPs on the surfaces. Through graphitization at 600, 800, and 1000 °C, the atomic and mass concentrations increase to 0.21% and 3.12%, 0.38% and 4.92%, and 0.95% and 8.04%, demonstrating the increased densities of exposed AuNPs on the surfaces of CNFs. Compared with the BEs of Au 4f of Au–PANFs (84.3 and 88.0 eV), the Au–CNFs graphitized at 600, 800, and 1000 °C exhibit lower BEs. With increased graphitization temperatures, the BEs of Au 4f get closer to the BEs of Au^0 (87.7 eV and 84.0 eV), suggesting the migration of AuNPs through the matrix of nanofibers. The changes in the mass concentration and atomic concentration of Au–PANFs and Au–CNFs-600, Au–CNFs-800 and Au–CNFs-1000 can strongly indicate the migration of AuNPs from the interior to the exterior of CNFs.

Fig. 6 shows the TEM and FE-TEM images of Au–CNFs with various graphitization temperatures at 600, 800 and 1000 °C, respectively. The heating rate of the graphitization process is 5 °C min^{-1}. As shown in Fig. 6a to c, a series of evolution can be clearly observed. With increased graphitization temperatures from 600 to 1000 °C, compared with the AuNPs embedded in PANFs (3.4 ± 0.6 nm), the average diameters of the AuNPs increased to 5.8 ± 1.1, 8.3 ± 2.3 and 10.2 ± 2.7 nm, respectively, which are similar to those shown in Fig. 6. In addition, compared with those of Au–PANFs (530 ± 52 nm), the diameters of Au–CNFs decrease to 306 ± 67, 234 ± 52, and 195 ± 48 nm, respectively, indicating the enormous shrinkage of nanofibers. The evolution of the migration of AuNPs can be clearly observed in the HRTEM images in Fig. 6a–c. At 600 °C, a little area of AuNPs is exposed and coated by three graphene layers, indicating the migration of AuNPs. Both the fringe of the AuNPs and graphitic carbon shells can be simultaneously observed in the insets of Fig. 6a. The lattice spacings of 0.23 nm and 0.36 nm are ascribed to the (111) plane of Au crystals and the (002) lattice plane of graphite, respectively.

Typically, upon increasing the temperature to 800 °C, more area of AuNPs are exposed from the interior of the nanofibers and coated by two graphene layers. With continuous increase to 1000 °C, the AuNPs are almost broken through the nanofibers and immobilized on the surfaces (Fig. 6c). The exposed AuNPs are also coated by two graphene layers. The complete migration process of AuNPs from the interior of PANFs to the exterior of CNFs can be clearly observed. The exposed AuNPs are surrounded by several graphene layers while the AuNPs embedded in PANFs are surrounded by large amounts of PAN macromolecules, which are consistent with the XPS results (Fig. 2). Note that as shown in Fig. 6c and f, more and more adjacent AuNPs formed, indicating the aggregation of AuNPs.

Table 1 XPS atomic concentrations, mass concentrations and Au 4f BEs of the Au–PANFs and CNFs graphitized at 600, 800, and 1000 °C min^{-1} at a heating rate of 2 °C min^{-1}

Samples	Au 4f binding energy (eV)	Atomic concentrations (%)	Mass concentrations (%)
Au–PANFs	84.3, 88.0	0.06	0.92
Au–CNFs-600	84.2, 87.9	0.21	3.12
Au–CNFs-800	84.2, 87.8	0.38	4.92
Au–CNFs-1000	84.1, 87.8	0.95	8.04

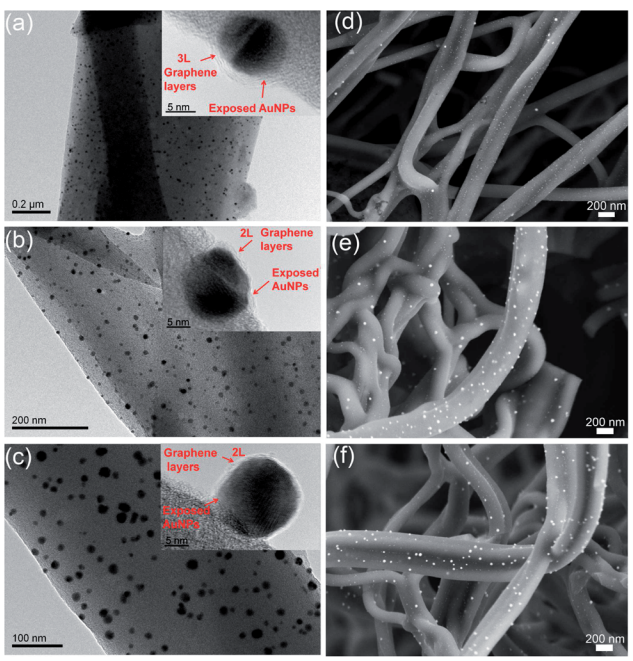

Fig. 6 TEM and FE-TEM images of Au–CNFs with various graphitization temperatures at (a and d) 600 °C, (b and e) 800 °C and (c and f) 1000 °C, respectively. Insets are the corresponding HRTEM images of the AuNPs. The heating rate of the graphitization process is 5 °C min^{-1}.

Published on 09 May 2014. Downloaded by Zhejiang Sci Tech University on 09/07/2014 13:10:12.

When the heating rate increased to 10 °C min^{-1}, as shown in Fig. 7a and d, the Au–CNFs (600 °C) exhibit high density of exposed AuNPs on the surfaces of CNFs. Compared with Au–PANFs, the average diameter of the AuNPs increases to 10.7 ± 2.8 nm and at this temperature and heating rate, the AuNPs still remain spherical. With the temperature increased to 800 °C, the exposed AuNPs tend to collide with adjacent NPs and grow up to larger sized AuNPs with irregular shape (Fig. 7b and e). Fig. 7c and f show the Au–CNFs carbonized at 1000 °C, and the spherical AuNPs embedded in PANFs grew up to larger sized AuNPs with irregular shapes immobilized on the CNFs, indicating the migration and ripening phenomena of AuNPs. The average diameter of the AuNPs with irregular shapes graphitized at 800 and 1000 °C are 18.2 ± 3.7 and 25.5 ± 5.1 nm. Compared with Au–PANFs, the diameter of Au–CNFs decreased to 260 nm ± 42, 205 ± 38 and 180 ± 36 nm, demonstrating the remarkable shrinkage of the nanofibers.

The heating temperature ranging from 300 to 500 °C belongs to the carbonization process. At a low heating rate (2 °C min^{-1}) and heating temperature (600 °C), the AuNPs with low exposed area have already emerged from the nanofibers (Fig. 6b). However, the AuNPs did not completely come out from the interior of nanofibers until the temperature increased to 1000 °C (Fig. 6d). However, at 1000 °C, the exposed AuNPs still remain small (6.9 ± 1.4 nm) and are uniformly spherical in shapewithout any aggregated NPs. Upon increasing the heating rate to 5 °C min^{-1}, the migration of AuNPs became faster in comparison with those shown in Fig. 7. The diameters of the AuNPs of Au–CNFs increase from 5.8 ± 1.1 to 10.2 ± 2.7 nm along with the increased heating temperatures from 600 to 800 °C, indicating that the faster heating rate results in the greater shrinkage and collisions of AuNPs to form larger sized AuNPs. Based on the above results, with the heating rate at 5 °C min^{-1} and graphitization temperature at 1000 °C, the AuNPs can completely expose on the surfaces of CNFs. Table 2 summarizes the statistics of the diameter of AuNPs embedded in PANFs and AuNPs immobilized on CNFs at different graphitization temperatures of 600, 800 and 1000 °C and heating rates of 2, 5, and 10 °C min^{-1}.

It can be concluded that the higher graphitization temperature and faster heating rate can strongly influence the shrinkage of the nanofibers and the sizes of AuNPs. In addition, the higher graphitization temperature and fast heating rate could result in the aggregation of AuNPs into larger ones that are inclined to be exposed on the surface of the CNFs. Therefore, these results can strongly support the assumption, that is, during the graphitization, with the conversion from amorphous structures to graphene layered structures, the pre-formed AuNPs embedded in PANFs can move around the randomly oriented graphene layers. Meanwhile, along with the shrinkage of nanofibers, the AuNPs can migrate to the surfaces of the CNFs.

To further investigate the migration of the AuNPs on the external surfaces of AuNPs, we performed a control experiment to count the number of AuNPs on CNFs. Fig. 8 shows the TEM and HAADF-STEM images of the Au–CNFs with low mass ratio of $HAuCl_4$ (0.5 wt%) treated at 1000 °C (5 °C min^{-1}). As shown in Fig. 8a, the AuNPs are evenly dispersed in the CNFs and however, it cannot be determined whether the AuNPs are embedded in the interior of CNFs or immobilized on the exterior of the CNFs. Focusing on the HAADF-STEM images of the Au–CNFs, it can be clearly observed that the AuNPs (bright spots) are indeed immobilized on the surfaces of the CNFs. The exposed density of the AuNPs in Fig. 8b is almost consistent with the AuNPs dispersed in CNFs in Fig. 8a. The STEM-EDS mapping images of the Au–CNFs taken randomly were to further investigate the locations of the AuNPs.

Fig. 8c shows the mapping area of the Au–CNFs and Fig. 8d exhibits the STEM-EDS mapping image of CNF constructed by

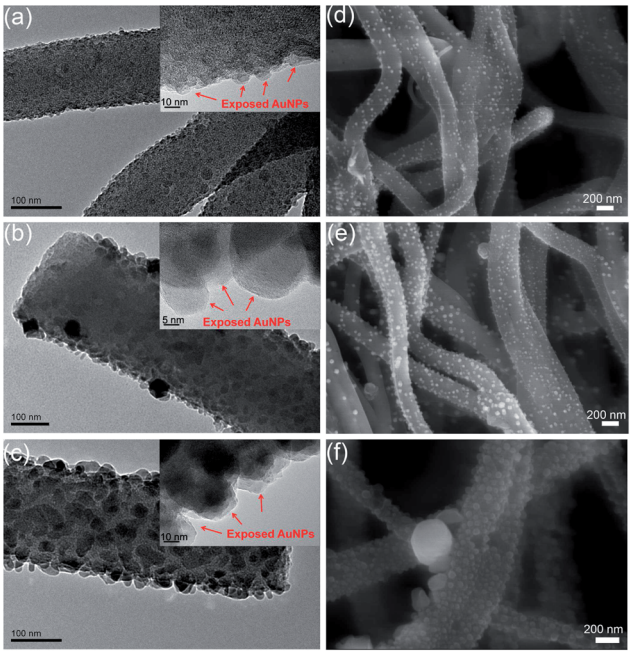

Fig. 7 TEM and FE-TEM images of Au–CNFs with various graphitization temperatures at (a and d) 600 °C, (b and e) 800 °C and (c and f) 1000 °C, respectively. Insets are the corresponding HRTEM images of the AuNPs. The heating rate of the graphitization process is 10 °C min^{-1}.

Table 2 The statistics of the AuNPs embedded in PANFs and AuNPs immobilized on CNFs at different graphitization temperatures and heating rates

Samples	Average diameters of AuNPs (nm)	Average diameters of nanofibers (nm)	Heating rates (°C min^{-1})
Au–PANFs	2.5 ± 0.6	530 ± 52	
Au–CNFs-600	4.1 ± 1.1	320 ± 64	2
Au–CNFs-800	4.9 ± 1.2	260 ± 43	2
Au–CNFs-1000	6.9 ± 1.4	210 ± 45	2
Au–CNFs-600	5.8 ± 1.1	306 ± 67	5
Au–CNFs-800	8.3 ± 2.3	234 ± 52	5
Au–CNFs-1000	10.2 ± 2.7	195 ± 48	5
Au–CNFs-600	10.7 ± 2.8	260 ± 42	10
Au–CNFs-800	18.2 ± 3.7	205 ± 38	10
Au–CNFs-1000	23.5 ± 5.1	180 ± 36	10

This journal is © The Royal Society of Chemistry 2014

Published on 09 May 2014. Downloaded by Zhejiang Sci Tech University on 09/07/2014 13:10:12.

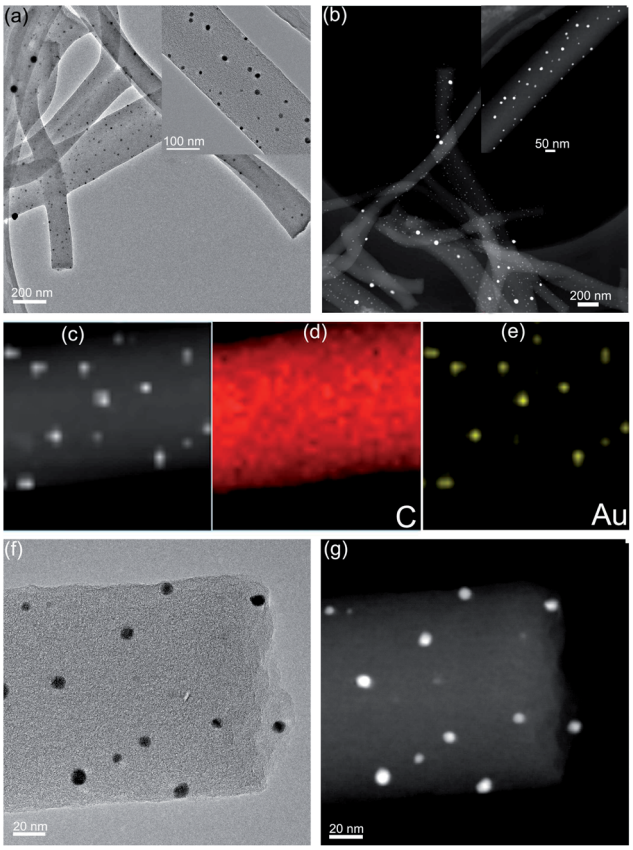

Fig. 8 (a) TEM and (b) HAADF-STEM images of the Au–CNFs graphitized at 1000 °C (5 °C min^{-1}) with low mass ratio of $HAuCl_4$ (0.5 wt%). Insets are the corresponding high-resolution TEM and HAADF-STEM images of single Au–CNFs. (c) HAADF-STEM and (d and e) STEM-EDS mapping images of the randomly selective area of the Au–CNFs. (f) TEM and (g) HAADF-STEM images of the Au–CNFs taken at the same areas.

carbon elements. Compared with the mapping area of CNFs in Fig. 8c, the yellow bright spots in Fig. 8e are constructed by Au elements and the shapes, locations and sizes are exactly the same. Twelve yellow spots (AuNPs) can be clearly observed, which are consistent with the number of the AuNPs in Fig. 8c, confirming the exposed AuNPs on the surfaces of CNFs. As shown in Fig. 8f, there are eleven AuNPs dispersed on CNFs. Compared with Fig. 8f, the HAADF-STEM image of the same area also exhibits eleven AuNPs with the same locations, shapes and sizes, locating on the surface of the CNF. Therefore, at a heating rate of 5 °C min^{-1} and graphitization temperature of 1000 °C, the initial AuNPs embedded in PANFs were migrated to the surfaces of CNFs.

On the basis of the above investigations, a schematic is displayed in Fig. 9 to summarize the behaviours of AuNPs migrated from the interior of PANFs to the external surfaces of CNFs during the graphitization process. According to our previous study, the small and well-dispersed AuNPs embedded in PANFs were synthesized by an *in situ* reduction approach.[41,42] The PAN macromolecule with abundant cyano groups (C≡N) can effectively anchor the AuNPs because of the strong chelating effect.[41,42] In addition, the PAN macromolecules both

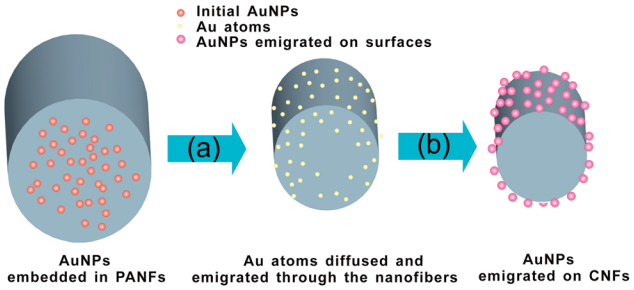

Fig. 9 Schematics of the behaviours of AuNPs migrated through the nanofibers during the graphitization process: (a) the melting of initial AuNPs embedded in PANFs and the diffusion and migration of Au atoms through the matrix of nanofibers. (b) The Au atoms diffused and migrated to the surfaces of the CNFs and grew up to AuNPs.

acted as chelating agents and stabilizers to protect the AuNPs from aggregations, leading to uniform and well-dispersed AuNPs. During the carbonization process, the C≡N structure started to get converted to the C=C–C=N structure, forming the aromatic structures and the graphene layer structures. Without the stabilization of the C≡N groups, the pre-formed AuNPs embedded in PANFs can migrate around the randomly oriented graphene layers.

It is reported that the metal NPs exhibit size-dependent meltings.[57] For particles of spherical geometry with diameter D:

$$T_m/T_b = 1 - C/D,$$

where T_m is the melting temperature of the NPs with diameter D, T_b is the melting temperature of bulk solids (Au: $T_b = 1338$ K), and C is the material constant (Au: $C = 1.1281$ nm). As discussed above, the average diameter of the initial AuNPs embedded in PANFs is 2.5 ± 0.6 nm and according to the equation, the melting temperature of the AuNPs is 734 K (461 °C), which is below the graphitization temperatures at 600 °C. Therefore, when AuNPs were treated at elevated temperatures, the initial AuNPs melted into an atom scale. The size of Au atoms is smaller than the spaces of graphene layers of the CNFs (0.37 nm) and therefore, the Au atoms can migrate and diffuse through the graphene layers. In our case, the randomly oriented graphene layers provide many potential paths (nanochannels) connecting the inner nanofibers and the external environment. However, these paths are not straight, but tortuous, thus, the distance for atoms to pass the nanofibers to the surfaces is largely exceeding the nanofiber thickness.

Under the same conditions, the Au atoms closer to the surfaces of nanofibers had smaller migratory distances and preferentially migrated to the surfaces. More and more preferentially migratory Au atoms were nucleated at the surfaces and grew up to NPs. The migration rates and diffusion of Au atoms were strongly dependent on the graphitization temperatures and heating rates. Higher graphitization temperatures and heating rates lead to faster molecular movement, indicating the faster migration and diffusion of Au atoms. Therefore, Au atoms with faster migration and diffusion rates get easily exposed on the surfaces of nanofibers, while the slower ones still remain in

Published on 09 May 2014. Downloaded by Zhejiang Sci Tech University on 09/07/2014 13:10:12.

the matrix of nanofibers. Along with the shrinkages of nanofibers, more and more Au atoms diffused and migrated to the surfaces of the CNFs and grew up to AuNPs. The larger size of AuNPs immobilized on CNFs was caused by the aggregation of the small AuNPs because of the faster diffusion of Au atoms during the carbonization process. Because of the high treatment temperature and the migration of the AuNPs, the neighboring AuNPs may collide with each other and then age to larger AuNPs.

To confirm this new strategy is a general approach for the fabrication of CNF–noble metal nanostructures, Pt–CNF hybrid nanostructures were also prepared by the method. As shown in Fig. 10a and c, the PtNPs with an average diameter of 4.4 ± 0.9 nm were evenly dispersed in the interior of PANFs. After graphitization at 1000 °C with the heating rate of 5 °C min^{-1}, most of the PtNPs were exposed on the surfaces of CNFs and the diameter of PtNPs increases to 10.7 ± 2.5 nm. The observed phenomena are similar to the Au–CNF systems, indicating that the new strategy is not only applicable to the Au system but also employed for the fabrication of other noble metal–CNF nanostructures.

Compared with the bulk metal electrode, such small, uniform and well-dispersed AuNPs immobilized on the surfaces of CNFs possess high ratio of surface atoms with free valences to the cluster of total atoms and can provide electrochemical reversibility for the redox reactions.[6,7] Fig. 11 shows the cyclic voltammograms (CVs) of CNFs and Au–CNF functionalized GCE with H_2O_2 in the presence of hydroquinone (HQ). According to the reported literature,[22,51] high graphitization temperatures would lead to the higher conductivity because of their increasing degree of graphitization of CNFs. Therefore, we investigated the electrochemical properties of CNFs and Au–CNFs with different graphitization temperatures and heating rates to study their morphology-dependent electrochemical activities. As shown in Fig. 11A, curve a is ascribed to the CVs of CNFs (graphitized at 1000 °C) with H_2O_2 in 5 mM HQ and much weak redox peaks can be observed. The curves b, c and d are ascribed to the CVs of Au–CNFs graphitized at 600, 800, and 1000 °C with a heating rate of 2 °C min^{-1}. Compared to the CVs

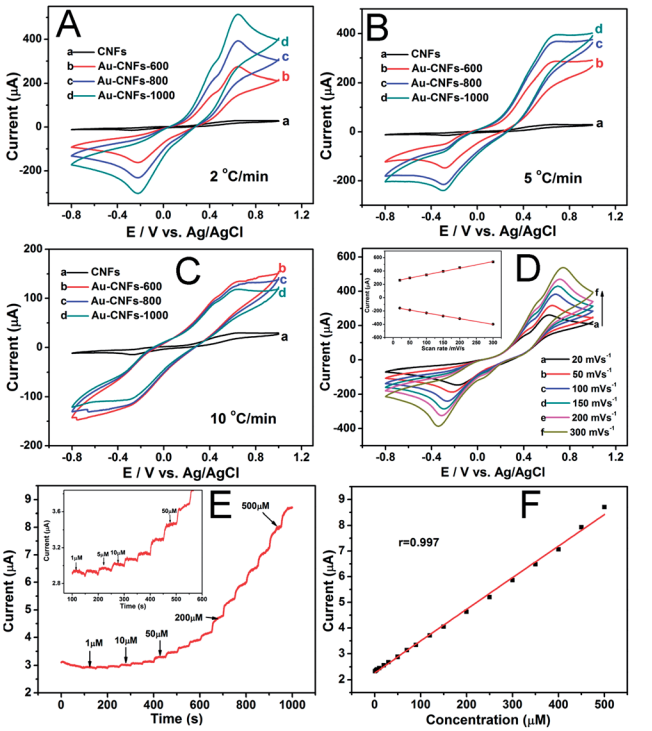

Fig. 11 (A–C) The electrochemical properties of CNFs and Au–CNFs with different graphitization temperatures and heating rates. CVs of (a) CNF/GCE, (b) Au–CNFs-600/GCE, (c) Au–CNFs-800/GCE and Au–CNFs-1000/GCE biosensor with 5.0 mM HQ in 0.1 M PBS in the presence of 5.0 mM H_2O_2 (scan rate, 50 mV s^{-1}). (D) CVs of Au–CNFs-1000/GCE (2 °C min^{-1}) in 1.0 mM H_2O_2 with different scan rates and the inset shows the relationship between the redox peak currents and scan rates; (E) amperometric response of the fabricated Au–CNFs-1000/GCE (2 °C min^{-1}) sensor to successive addition of different concentrations of H_2O_2 to 1.0 M PBS and the inset shows the response of the sensor from 1 μM to 50 μM H_2O_2; and (F) relationship of the calibration curve and the linear fitting curve between the currents and the H_2O_2 concentration.

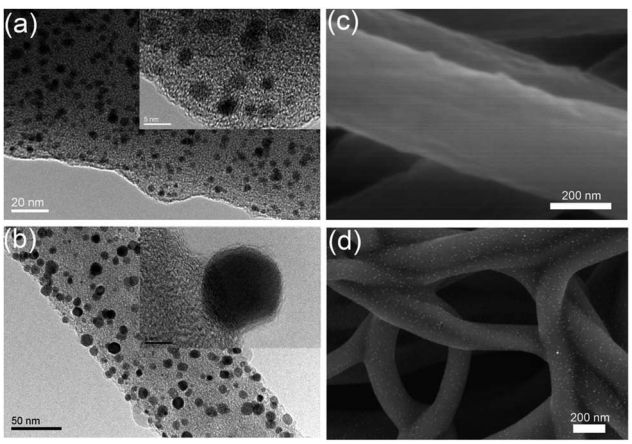

Fig. 10 TEM and FE-SEM images of the (a and c) Pt–PANFs and (b and d) Pt–CNFs (1000 °C, 5 °C min^{-1}) hybrid nanostructures. Insets are the corresponding HRTEM images.

of CNFs (curve a) with Au–CNFs in HQ with H_2O_2 (curve b to d), significant redox peaks of Au–CNFs are obtained, indicating the electroactive property of Au–CNFs. It can be clearly observed that even the sizes of the AuNPs on CNFs increased from 4.1 to 6.9 nm, the intensity of the redox peaks significantly increased with the increased density of exposed AuNPs (Fig. 11A, curve b to d). The Au–CNFs-1000 with high density of exposed AuNPs possesses higher specific surface area and active sites. It means that more AuNPs will take part in the reactions, leading to the higher electrocatalytic activity. The redox peak currents of HQ (curve d) are about 298.4 and 511.6 μA, with potentials at −0.22 and 0.65 V, respectively. When the Au–CNFs were treated by a relatively high heating rate (5 °C min^{-1}), the sizes of the AuNPs on CNFs increased from 5.8 to 10.2 nm and the redox peaks of HQ still exhibit a similar trend (Fig. 11B). However, when the heating rate increased to 10 °C min^{-1}, Fig. 11C indicates an inverse phenomenon that the intensities of the redox peaks of HQ decreased with the graphitization temperature. The sizes of the AuNPs on CNFs increased from 10.7 to 23.5 nm and more serious aggregated AuNPs can be found, resulting in the weak

This journal is © The Royal Society of Chemistry 2014

Published on 09 May 2014. Downloaded by Zhejiang Sci Tech University on 09/07/2014 13:10:12.

Table 3 Summary of the response time, detection range, and detection time of as-prepared H_2O_2 electrochemical sensors in comparison with other reported sensors

Electrochemical sensor	Response time (s)	Detecion range (μM)	Detecion limit (μM)	Ref.
Au–CNFs	1	1–500	0.42	This work
HRP–AuNP–PVA	1	1–500	0.5	58
HRP–AgNP–PVA/PEI	2	5–550	2.5	30
HRP–Ag–PVA	2	10–560	5.6	31
HRP–AuNP cellulose NFs	1	1–500	1	59
HRP–Fe_3O_4–silica	No data	2–24	0.43	60
HRP–sonogel–carbon	No data	4–100	1.6	61

electrochemical activity of AuNPs. The increased density of the AuNPs on CNFs cannot offset the decrease in the activities of AuNPs caused by the larger size and aggregation.

Therefore, slower heating rates (2–5 °C min^{-1}) would lead to a small increase in the sizes of AuNPs (below 10 nm) and the higher graphitization temperatures would bring about the higher exposed density of AuNPs on the surfaces of CNFs (600–1000 °C). The synergistic effects between the smaller size and higher exposed density of AuNPs lead to the increased electrochemical activity. Because of the highest electrochemical activity, we use the Au–CNFs-1000/GCE (2 °C min^{-1}) to evaluate the detection limits of the constructed biosensors. Fig. 11D exhibits CV curves of Au–CNFs-1000 (2 °C min^{-1}) at different scan rates ranging from 20 to 300 mV s^{-1}. It is obvious that the shape of the CVs almost does not change in the range varied from 20 to 300 mV s^{-1} and the total peak current density increases with increasing potential scan rates, which demonstrates a good rate property and excellent electrochemical behavior for the Au–CNFs-1000 (2 °C min^{-1}) functionalized electrode. Meanwhile, the inset in Fig. 11B shows that there is a linear relationship between the redox peak current density and the scan rate for the electrode materials, indicating that the electrode process is a surface-controlled process.

For the amperometric sensing application, the Au–CNFs-1000 (2 °C min^{-1}) functionalized GCE electrodes are generally evaluated by measuring the current response at a working potential of 0.0 V for the detection of H_2O_2. Fig. 11E displays the amperometric response at the CNFs and the Au–CNFs-1000 (2 °C min^{-1}) modified GCE towards the successive addition of H_2O_2. As shown in Fig. S2,† the CNF/GCE exhibits a weaker response to the addition of H_2O_2, while the Au–CNF/GCE shows a larger catalytic current to the changes of the H_2O_2 concentration (Fig. 11E). The rapid electrode response to the change of the H_2O_2 concentration could be attributed largely to the well-dispersed AuNPs immobilized on the Au–CNFs, which could effectively promote the electron transfer rate between the H_2O_2 and the electrode. With the continued addition of H_2O_2, the sensor responded rapidly to the substrates and could achieve 90% of the steady-state current within 3 s, indicating the fast amperometric response to the reduction of H_2O_2. Fig. 11F shows a linear relationship of the concentration of H_2O_2 with the correlation coefficient of 0.997. The detection limit of 0.42 μM was estimated at a signal-to-noise ratio of 3.

Most of the biosensors for the detection of H_2O_2 should be assisted by immobilizing the horseradish peroxidase (HRP). In our present investigations, the constructed nonenzymatic sensors show lower detection limit and wider responding range for H_2O_2 without any enzyme. Table 3 summaries the response time, detection range, and detection time of as-prepared H_2O_2 electro-chemical sensors in comparison with other reported sensors. It is can be clearly observed that our sensors without any enzyme exhibit lower detection limits and faster response than those systems with HRP as reported in the literature.

In addition, the Au–CNF electrochemical sensors exhibit good reproducibility in the detection of H_2O_2 with a relative standard deviation (RSD) of about 3.3% in the presence of 5.0 mM of H_2O_2 obtained by recycling for more than 10 measurements. The fabricated Au–CNF electrodes used 10 times were compared by the CV curves (Fig. S3†) and the redox peaks are almost the same, indicating the excellent stability and reusability of electrochemical sensors. The sensors show lower detection limit and wider responding range, indicating that the fabricated sensor could be potentially used for monitoring the concentration of H_2O_2 without any enzyme.

Conclusions

A novel strategy for the design of novel nanostructures to show an unexpected behavior of AuNPs embedded in the interior of PANFs, which can migrate to the external surfaces of the CNFs during the graphitization process have been demonstrated. With the conversion from the amorphous structures of PANFs to graphene layered structures of CNFs, the initial AuNPs embedded in the interior of the PANFs migrate to the external surfaces of CNFs. The migration of AuNPs through the nanofiber matrix are strongly dependent on the graphitization temperature and heating rates. Three different heating rates at 2, 5, and 10 °C min^{-1} and graphitization temperatures at 600, 800, and 1000 °C, respectively, were performed to investigate the migration and the exposed density of AuNPs on the CNFs. In addition, the conversion in the chemical structures from the C≡N structure to the C=C–C=N structure during the graphitization process was investigated. The migration phenomena of AuNPs are explained by an atom diffusion mechanism. These novel nanomaterials were constructed as a nonenzymatic H_2O_2 electrochemical sensor. The electrochemical sensors based on AuNPs with different densities of exposed AuNPs exhibit significant promoted electrochemical activity with increased density of exposed AuNPs. The Au–CNFs with high density of exposed AuNPs possess higher specific surface area and active

Published on 09 May 2014. Downloaded by Zhejiang Sci Tech University on 09/07/2014 13:10:12.

sites. It means that more AuNPs will take part in the reactions, leading to higher electrocatalytic activity. The sensor showed lower detection limit and wider responding range, indicating that the fabricated sensor could be potentially used for monitoring the concentration of H_2O_2 without any enzyme. The present investigations provide a general route for the fabrication of nanostructures for novel electrochemical sensors, energy storage devices and so on.

Acknowledgements

This work was supported by the National Natural Science Foundation of China (NSFC) (51373154), the 521 Talent Project of Zhejiang Sci-Tech University and the Key Discipline Open Fund of the Zhejiang Province (2014KF01).

Notes and references

1 X. Y. Lang, H. Y. Fu, C. Hou, G. F. Han, P. Yang, Y. B. Liu and Q. Jiang, *Nat. Commun.*, 2013, **4**, 2169.
2 P. Lin and F. Yan, *Adv. Mater.*, 2012, **24**, 34–51.
3 C. Marichy, M. Bechelany and N. Pinna, *Adv. Mater.*, 2012, **24**, 1017–1032.
4 L. Matlock-Colangelo and A. J. Baeumner, *Lab Chip*, 2012, **12**, 2612–2620.
5 Y. Q. Wang, B. Yan and L. X. Chen, *Chem. Rev.*, 2013, **113**, 1391–1428.
6 L. N. Cella, W. Chen, N. V. Myung and A. Mulchandani, *J. Am. Chem. Soc.*, 2010, **132**, 5024–5026.
7 X. M. Feng, R. M. Li, Y. W. Ma, R. F. Chen, N. E. Shi, Q. L. Fan and W. Huang, *Adv. Funct. Mater.*, 2011, **21**, 2989–2996.
8 Y. D. Jin, *Adv. Mater.*, 2012, **24**, 5153–5165.
9 S. Myung, A. Solanki, C. Kim, J. Park, K. S. Kim and K. B. Lee, *Adv. Mater.*, 2011, **23**, 2221–2225.
10 R. J. Chen, H. C. Choi, S. Bangsaruntip, E. Yenilmez, X. W. Tang, Q. Wang, Y. L. Chang and H. J. Dai, *J. Am. Chem. Soc.*, 2004, **126**, 1563–1568.
11 H. Im, X. J. Huang, B. Gu and Y. K. Choi, *Nat. Nanotechnol.*, 2007, **2**, 430–434.
12 Y. Xiang and Y. Lu, *Nat. Chem.*, 2011, **3**, 697–703.
13 N. J. Ronkainen, H. B. Halsall and W. R. Heineman, *Chem. Soc. Rev.*, 2010, **39**, 1747–1763.
14 J. Wang, *Chem. Rev.*, 2008, **108**, 814–825.
15 S. Mao, G. H. Lu, K. H. Yu, Z. Bo and J. H. Chen, *Adv. Mater.*, 2010, **22**, 3521–3526.
16 J. Lu, I. Do, L. T. Drzal, R. M. Worden and I. Lee, *ACS Nano*, 2008, **2**, 1825–1832.
17 A. L. Torre, M. D. C. Gimenez-Lopez, M. W. Fay, G. A. Rance, W. A. Solomonsz, T. W. Chamberlain, P. D. Brown and A. N. Khlobystov, *ACS Nano*, 2012, **6**, 2000–2007.
18 K. Besteman, J. O. Lee, F. G. M. Wiertz, H. A. Heering and C. Dekker, *Nano Lett.*, 2003, **3**, 727–730.
19 J. Wang, M. Musameh and Y. H. Lin, *J. Am. Chem. Soc.*, 2003, **125**, 2048–2049.
20 J. B. Mu, C. L. Shao, Z. C. Guo, Z. Y. Zhang, M. Y. Zhang, P. Zhang, B. Chen and Y. C. Liu, *ACS Appl. Mater. Interfaces*, 2011, **3**, 590–596.
21 A. Stein, Z. Y. Wang and M. A. Fierke, *Adv. Mater.*, 2009, **21**, 265–293.
22 X. W. Mao, F. Simeon, G. C. Rutledge and T. A. Hatton, *Adv. Mater.*, 2013, **25**, 1309–1314.
23 A. Greiner and J. H. Wendorff, *Angew. Chem., Int. Ed.*, 2007, **46**, 5670–5703.
24 L. W. Ji, O. Toprakci, M. Alcoutlabi, Y. F. Yao, Y. Li, S. Zhang, B. K. Guo, Z. Lin and X. W. Zhang, *ACS Appl. Mater. Interfaces*, 2012, **4**, 2672–2679.
25 X. F. Lu, X. J. Bian, G. D. Nie, C. C. Zhang, C. Wang and Y. Wei, *J. Mater. Chem.*, 2012, **22**, 12723–12730.
26 P. Q. Wang, D. Zhang, F. Y. Ma, Y. Ou, Q. N. Chen, S. H. Xie and J. Y. Li, *Nanoscale*, 2012, **4**, 7199–7204.
27 J. S. Bonso, G. D. Kalaw and J. P. Ferraris, *J. Mater. Chem. A*, 2014, **2**, 418–424.
28 M. R. Langille, M. L. Personick and C. A. Mirkin, *Angew. Chem., Int. Ed.*, 2013, **52**, 13910–13940.
29 A. S. Urban, X. S. Shen, Y. M. Wang, N. Large, H. Wang, M. W. Knight, P. Nordlander, H. Y. Chen and N. J. Halas, *Nano Lett.*, 2013, **13**, 4399–4403.
30 H. Zhu, M. L. Du, M. Zhang, P. Wang, S. Y. Bao, L. N. Wang, Y. Q. Fu and J. M. Yao, *Biosens. Bioelectron.*, 2013, **49**, 210–215.
31 H. Zhu, M. L. Du, M. Zhang, P. Wang, S. Y. Bao, Y. Q. Fu and J. M. Yao, *Sens. Actuators, B*, 2013, **185**, 608–619.
32 H. Zhu, M. Zhang, S. Y. Cai, Y. T. Cai, P. Wang, S. Y. Bao, M. L. Zou and M. L. Du, *RSC Adv.*, 2014, **4**, 794–804.
33 H. Zhu, M. L. Du, M. Zhang, P. Wang, S. Y. Bao, M. L. Zou, Y. Q. Fu and J. M. Yao, *Biosens. Bioelectron.*, 2014, **54**, 91–101.
34 J. Li, S. B. Tang, L. Lu and H. C. Zeng, *J. Am. Chem. Soc.*, 2007, **129**, 9401–9409.
35 I. Kvande, J. Zhu, T. J. Zhao, N. Hammer, M. Ronning, S. Raaen, J. C. Walmsley and D. Chen, *J. Phys. Chem. C*, 2010, **114**, 1752–1762.
36 D. Y. Shin, B. Jeong, B. S. Mun, H. Jeon, H. J. Shin, J. Baik and J. Lee, *J. Phys. Chem. C*, 2013, **117**, 11619–11624.
37 S. Hermans, V. Bruyr and M. A. Devillers, *J. Mater. Chem.*, 2012, **22**, 14479–14486.
38 C. H. Liang, W. Xia, M. V. D. Berg, Y. M. Wang, H. Soltani-Ahmadi, O. Schluter, R. A. Fischer and M. Muhler, *Chem. Mater.*, 2009, **21**, 2360–2366.
39 Z. X. Yang, G. D. Du, Z. P. Guo, X. B. Yu, S. Li, Z. X. Chen, P. Zhang and H. K. Liu, *Nanoscale*, 2010, **2**, 1011–1017.
40 H. Q. Hou and D. H. Reneker, *Adv. Mater.*, 2004, **16**, 69–73.
41 H. Zhu, M. L. Du, M. L. Zou, C. S. Xu, N. Li and Y. Q. Fu, *J. Mater. Chem.*, 2012, **22**, 9301–9307.
42 M. L. Zou, M. L. Du, H. Zhu, C. S. Xu, N. Li and Y. Q. Fu, *Polym. Eng. Sci.*, 2013, **53**, 1099–1108.
43 L. J. Wang, J. H. Hu, H. Y. Zhang and T. Zhang, *Chem. Commun.*, 2011, **47**, 6837–6839.
44 C. Y. Su, Y. F. Tong, M. Y. Zhang, Y. Zhang and C. L. Shao, *RSC Adv.*, 2013, **3**, 7503–7512.
45 Y. Aykut, *ACS Appl. Mater. Interfaces*, 2012, **4**, 3405–3415.
46 B. S. Lee, S. B. Son, K. M. Park, G. S. Lee, K. H. Oh, S. H. Lee and W. R. Yu, *ACS Appl. Mater. Interfaces*, 2012, **4**, 6702–6710.
47 Z. C. Xu, Y. L. Hou and S. H. Sun, *J. Am. Chem. Soc.*, 2007, **129**, 8698–8699.

 This journal is © The Royal Society of Chemistry 2014

Published on 09 May 2014. Downloaded by Zhejiang Sci Tech University on 09/07/2014 13:10:12.

48 H. Zhu, M. L. Du, D. L. Yu, Y. Wang, L. N. Wang, M. L. Zou, M. Zhang and Y. Q. Fu, *J. Mater. Chem. A*, 2013, **1**, 919–929.
49 Y. Negishi, K. Nobusada and T. Tsukuda, *J. Am. Chem. Soc.*, 2005, **127**, 5261–5270.
50 A. Tanaka, Y. Takeda, M. Imamura and S. Sato, *Phys. Rev. B: Condens. Matter Mater. Phys.*, 2003, **68**, 195415.
51 W. Li, L. S. Zhang, Q. Wang, Y. Yu, Z. Chen, C. Y. Cao and W. G. Song, *J. Mater. Chem.*, 2012, **22**, 15342–15347.
52 J. Q. Wang, K. Pan, E. P. Giannelis and B. Cao, *RSC Adv.*, 2013, **3**, 8978–8987.
53 A. G. El-Deen, N. A. M. Barakat, K. A. Khalil and H. Y. Kim, *J. Mater. Chem. A*, 2013, **1**, 11001–11010.
54 M. Zhang, E. Uchaker, S. Hu, Q. F. Zhang, T. H. Wang, G. Z. Cao and J. Y. Li, *Nanoscale*, 2013, **5**, 12342–12349.
55 J. N. Wang, W. Qin, X. Q. Liu and H. Q. Liu, *RSC Adv.*, 2013, **3**, 11132–11139.
56 W. B. Li, Z. H. Yang, G. L. Zhang and Q. Meng, *Ind. Eng. Chem. Res.*, 2013, **52**, 6492–6501.
57 K. K. Nanda, S. N. Sahu and S. N. Behera, *Phys. Rev. A: At., Mol., Opt. Phys.*, 2002, **66**, 013208.
58 J. Wang, H. B. Yao, D. He, C. L. Zhang and S. H. Yu, *ACS Appl. Mater. Interfaces*, 2012, **4**, 1963–1971.
59 T. Zhang, W. Wang, D. Zhang, X. Zhang, Y. Ma, Y. Zhou and L. Qi, *Adv. Funct. Mater.*, 2010, **20**, 1152–1160.
60 Y. H. Won, D. Aboagye, H. S. Jang, A. Jitianu and L. A. Stanciu, *J. Mater. Chem.*, 2010, **20**, 5030–5034.
61 J. L. H. H. de Cisneros, M. Elkaoutit, I. Naranjo-Rodriguez, M. Dominguez, M. P. Hernandez-Artiga and D. Bellida-Milla, *Electrochim. Acta*, 2008, **53**, 7131–7137.